NANO LETTERS

pubs.acs.org/NanoLett Letter

# Integrated Terahertz Generator-Manipulators Using Epsilon-near-Zero-Hybrid Nonlinear Metasurfaces

Yongchang Lu,† Xi Feng,† Qingwei Wang,† Xueqian Zhang,* Ming Fang,* Wei E.I. Sha, Zhixiang Huang, Quan Xu, Li Niu, Xieyu Chen, Chunmei Ouyang, Yuanmu Yang, Xixiang Zhang, Eric Plum, Shuang Zhang,* Jiaguang Han,* and Weili Zhang

Cite This: *Nano Lett.* 2021, 21, 7699−7707 Read Online

ACCESS | Metrics & More | Article Recommendations | Supporting Information

**ABSTRACT:** In terahertz (THz) technologies, generation and manipulation of THz waves are two key processes usually implemented by different device modules. Integrating THz generation and manipulation into a single compact device will advance the applications of THz technologies in various fields. Here, we demonstrate a hybrid nonlinear plasmonic metasurface incorporating an epsilon-near-zero (ENZ) indium tin oxide (ITO) layer to seamlessly combine efficient generation and manipulation of THz waves across a wide frequency band. The coupling between the plasmonic resonance of the metasurface and the ENZ mode of the ITO thin film enhances the THz conversion efficiency by more than 4 orders of magnitude. Meanwhile, such a hybrid device is capable of shaping the polarization and wavefront of the emitted THz beam via the engineered nonlinear Pancharatnam-Berry (PB) phases of the plasmonic meta-atoms. The presented hybrid nonlinear metasurface opens a new avenue toward miniaturized integrated THz devices and systems with advanced functionalities.

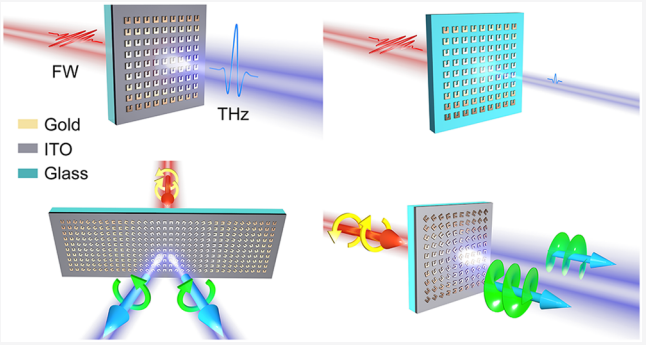


**KEYWORDS:** *terahertz, integrated generator-manipulator, metasurface, epsilon-near-zero, nonlinear Pancharatnam-Berry phase*



Terahertz (THz) technology has been playing an increasingly important role in various fields including spectroscopy, imaging, sensing, and communications.[1] To facilitate these THz applications, high-performance devices for both THz generation and manipulation are highly desired. Over the last two decades, various methods have been developed for THz generation, such as those based on nonlinear organic crystals,[2,3] spintronic films,[4,5] topological materials,[6,7] and resonance-enhanced photoconductive antennas.[8] Recent progress in metasurfaces has allowed for effective control of polarization and wavefront of terahertz waves.[9−15] However, in most THz systems demonstrated thus far, devices for generating and manipulating THz waves are spatially separated, while integrating these two essential functions into a single device, i.e., an integrated generator-manipulator (IGM), will lead to lower-cost and more-compact THz systems. This will significantly advance the current THz devices and technologies.

The emergence of nonlinear metasurfaces provides a promising solution by controlling both the linear and nonlinear responses to electromagnetic waves. As a nonlinear extension of linear metasurfaces, which manipulate the amplitude, phase, polarization, and wavefront of fundamental waves (FWs),[16,17] nonlinear metasurfaces provide unprecedented functionalities to control and enhance nonlinear light-matter interactions,[18,19] such as second- and third-harmonic generation,[20−22] and THz generation via difference frequency generation.[23−25] More interestingly, nonlinear metasurfaces can steer the generated nonlinear wave through judiciously engineered symmetry and geometry of the meta-atoms. Therefore, nonlinear metasurfaces provide a multifunctional platform for generating and manipulating THz waves simultaneously. However, due to the deeply subwavelength interaction length, practical applications of nonlinear metasurfaces have been hampered by a very low conversion efficiency.

Attempts have been made to enhance the conversion efficiency of nonlinear metasurfaces while maintaining their ultrathin geometry. One approach is to apply materials with large nonlinearities, such as III−V semiconductors,[22] multi-quantum-well structures,[26] and nonlinear crystals;[27] another one is to enhance the fields of the fundamental pump wave and the generated nonlinear wave by using photonic engineering,

**Received:** June 28, 2021
**Published:** September 9, 2021

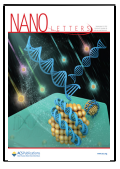




https://doi.org/10.1021/acs.nanolett.1c02372
*Nano Lett.* 2021, 21, 7699−7707

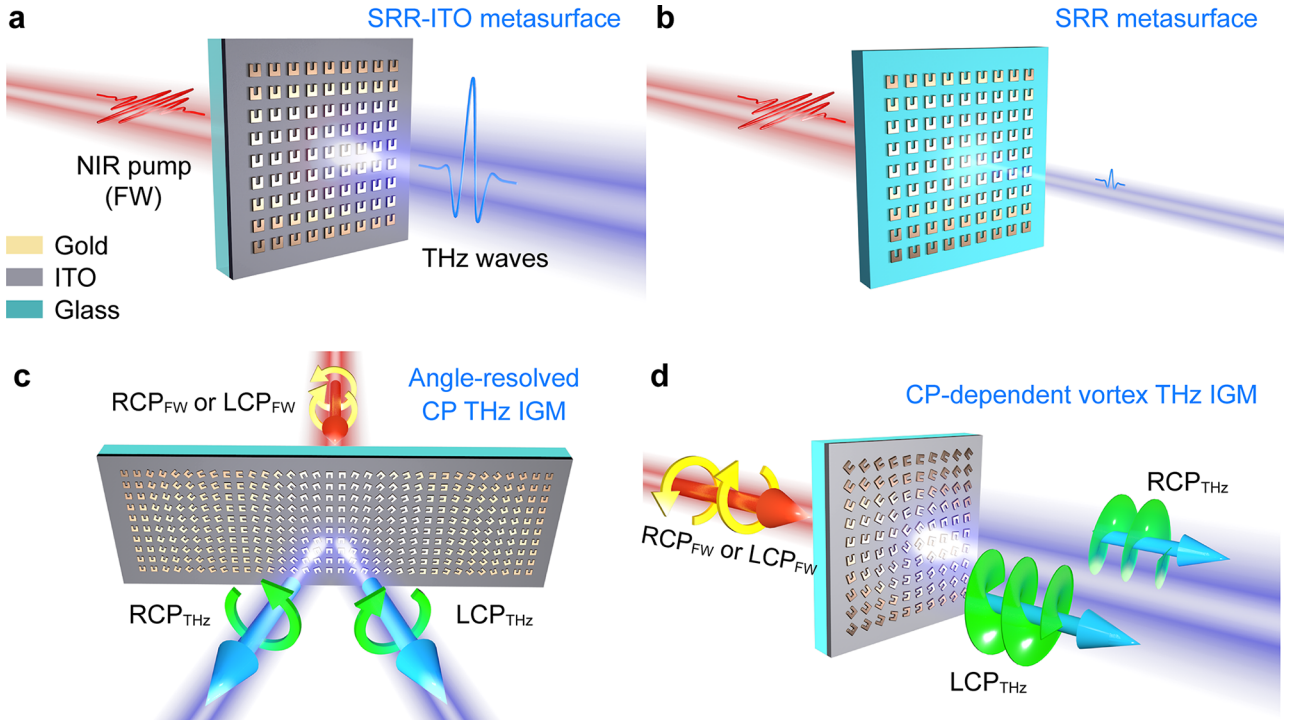


**Figure 1.** Enhanced THz generator and integrated generator manipulators. (a) SRR-ITO metasurface. (b) SRR metasurface without ITO as control sample. Upon resonant pumping with NIR femtosecond laser pulses and compared to the SRR metasurface, the SRR-ITO metasurface yields an $\sim 1 \times 10^4$ times enhancement of the peak THz intensity, serving as an enhanced THz generator. (c) Broadband angle-resolved CP THz IGM (IGM1), which emits different CP THz waves toward different directions under CP pumping. (d) Broadband CP-dependent vortex THz IGM (IGM2), which emits CP THz beams carrying different orbital angular momenta under CP pumping. In c and d, the emission directions, polarizations, and topological charges of the generated THz beams do not depend on the handedness of the CP NIR fundamental wave.

based on a number of effects such as Fano resonances,[21,28] bound states in the continuum (BICs) resonances,[22,29] and surface lattice effects.[30,31] Recently, epsilon-near-zero (ENZ) films,[32,33] including indium tin oxide (ITO),[34,35] aluminum-doped zinc oxide (AZO),[36,37] and indium-doped cadmium oxide (CdO)[38] films, have emerged as promising alternatives for enhancing nonlinear effects, benefiting from the extremely large field enhancement arising from the continuity of the normal displacement field across the ENZ interface. Hybridizing metasurfaces with ENZ films could further boost the nonlinearity by leveraging the strong near-field distribution of the resonant meta-atoms at desired frequencies.[39−41]

In this article, we design an ENZ-film-based hybrid nonlinear metasurface as a THz source to simultaneously generate and manipulate THz waves. The metasurface is composed of nanoscale plasmonic meta-atoms in the form of split-ring resonators (SRRs), fabricated on an ultrathin ENZ ITO film. Both the plasmonic resonance mode of the SRR and the ENZ mode of the ITO film are spatially overlapped and spectrally matched to achieve strong mode coupling. Thus, a pronounced nonlinear response occurs in the near-infrared (NIR) spectral range. Presence of the ITO film yields $\sim 1 \times 10^4$ times enhancement of the generated peak THz intensity under the same NIR pumping, as schematically illustrated in Figure 1a, b. Moreover, simultaneous polarization and wavefront manipulations of the emitted THz waves are implemented using such a hybrid configuration. Two THz IGMs are demonstrated to respectively produce angle-resolved circularly polarized (CP) THz waves (see Figure 1c) and CP-dependent vortex THz waves (see Figure 1d) through manipulating the nonlinear Pancharatnam-Berry (PB) phase of the plasmonic meta-atoms. All the devices show broadband THz generation spanning over 2 THz, whereas the conversion efficiency is comparable to that of a ZnTe crystal of 0.2 mm thickness under the same pumping conditions. Our work offers a new route toward developing novel integrated THz functional devices.

## RESULTS

**ITO Film and Meta-Atom Design.** Ultrathin ITO film is an ENZ material that exhibits large optical nonlinearity.[34,42] The large nonlinearity is attributed to the strong field confinement associated with the Ferrell-Berreman mode or the ENZ mode, which has a nearly flat dispersion near the ENZ wavelength.[43,44] However, the confined mode can only enhance the field component perpendicular to the film and thus cannot be excited without any near-field coupling under normal illumination. Here, we employ plasmonic resonant meta-atoms to fulfill such an excitation so as to boost the nonlinear response in ITO for THz generation by utilizing the field enhancement effects of the plasmonic resonance and the ENZ mode. We use a commercially available amorphous ITO film of 23 nm thickness on a float glass of 700 $\mu$m thickness (PGO GmbH), which has an ENZ wavelength $\lambda_{ENZ}$ around 1432 nm according to spectroscopic ellipsometry.

Figure 2a shows the unit cell of the hybrid nonlinear metasurface, which contains a split-ring resonator (SRR) on top of the ITO film. A 1.0 mm × 1.0 mm uniform array of such unit cells on ITO film and a control sample of the same configuration but without the ITO film were fabricated (see Methods). The two samples are named "SRR-ITO" metasurface and "SRR" metasurface, respectively, in the subsequent


https://doi.org/10.1021/acs.nanolett.1c02372
Nano Lett. 2021, 21, 7699−7707

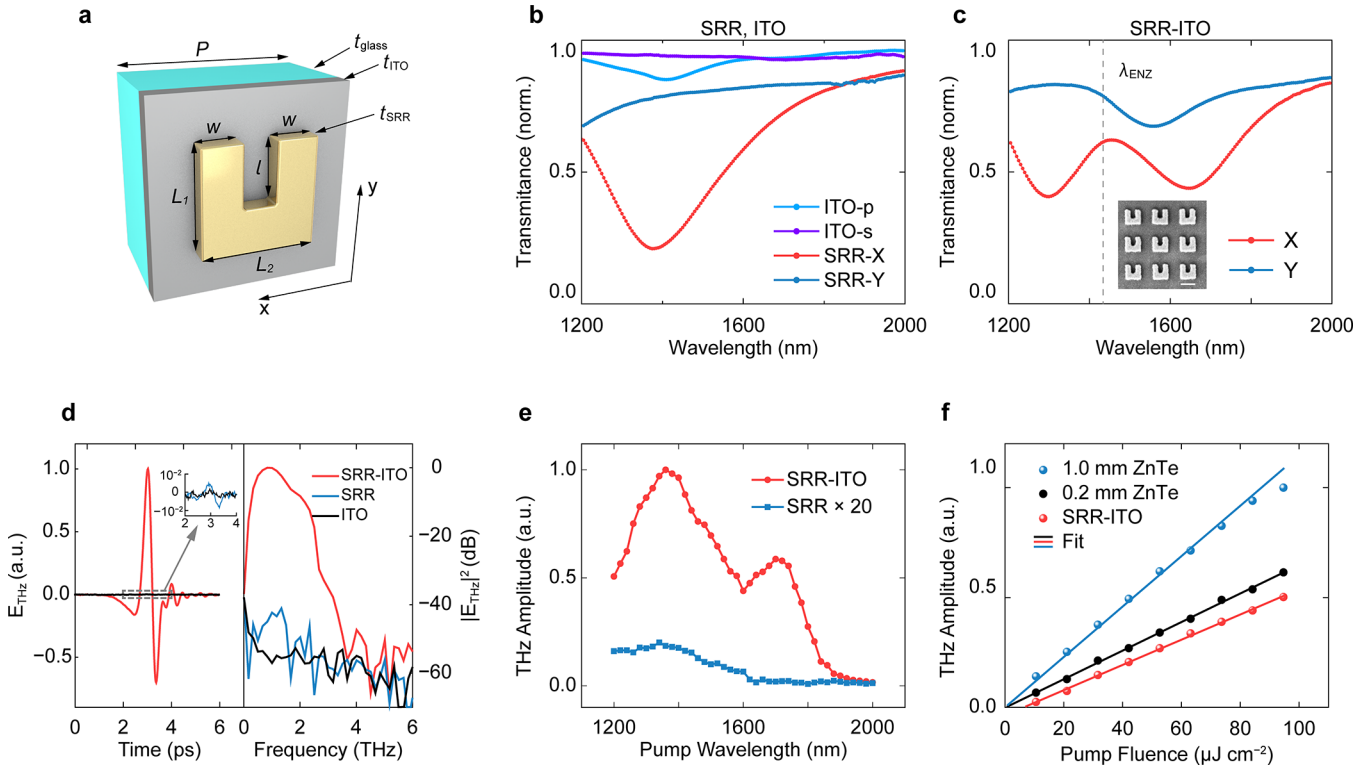


**Figure 2.** Hybrid nonlinear metasurface and enhanced THz generation. (a) Schematic of the unit cell of the SRR-ITO metasurface with $L_1$ = 212 nm, $L_2$ = 220 nm, $l$ = 122 nm, $w$ = 79 nm, $t_{SRR}$ = 40 nm, $t_{ITO}$ = 23 nm, $t_{glass}$ = 700 $\mu$m, and $P$ = 382 nm, respectively. (b, c) Measured transmission spectra of the SRR and the SRR-ITO metasurfaces under $x$-polarized and $y$-polarized illumination at normal incidence and bare ITO film under $s$-polarized and $p$-polarized illumination at 45° oblique incidence, respectively. In c, the inset shows a scanning electron microscope image of a fragment of the fabricated SRR-ITO metasurface (scale bar: 200 nm) and the dashed line represents the ENZ wavelength $\lambda_{ENZ}$. (d) Measured normalized time-domain THz pulses (left) and the corresponding normalized Fourier-transformed (frequency-domain) spectra (right) from the SRR-ITO metasurface, the SRR metasurface, and the bare ITO film under normal pumping at 1432 nm wavelength. The inset in left shows the results in the dashed box enlarged. (e) Measured pump-wavelength-dependent peak-to-peak amplitudes of THz pulses from the SRR-ITO metasurface and the SRR metasurface under normal pumping. (f) Comparison of the pump-fluence-dependent peak-to-peak amplitudes of THz pulses from the SRR-ITO metasurface and a 0.2 mm thick 110-cut ZnTe crystal under normal pumping at 1360 nm wavelength, as well as a 1.0 mm thick 110-cut ZnTe crystal under normal pumping at 800 nm wavelength.

discussion. Their measured polarization-dependent transmission spectra are shown in Figure 2b, c (see Methods). Without the ITO film, a strong resonance occurs at 1375 nm wavelength under $x$-polarized illumination, which corresponds to the magnetic dipole resonance of the SRRs. The resonance of the SRR metasurface is designed to be closely aligned to $\lambda_{ENZ}$. Addition of the ITO film, however, strongly modifies the transmission spectrum. A resonance splitting is observed under $x$-polarized illumination, with one transmission dip located at 1300 nm and the other at 1645 nm wavelength. Meanwhile, a pronounced transparency window emerges around $\lambda_{ENZ}$, as denoted by the dashed line in Figure 2c. This Fano-like spectral feature resembles that of plasmon-induced transparency, where the magnetic dipole resonance of the SRR and the ENZ mode of the ITO film function as the bright and dark modes, respectively (see Supporting Information Note 1). To show the dark mode of the ITO film, we plot in Figure 2b the measured polarization-dependent transmission spectra of an identical but bare ITO film at 45° oblique incidence. Under $s$-polarized illumination, no resonance feature is observed due to the lack of perpendicular field component. A similar result can also be found at normal incidence. Under $p$-polarized illumination, however, a resonance dip occurs around $\lambda_{ENZ}$ that is due to the ENZ effect. In the SRR-ITO metasurface, the resonance of the SRR contains rich perpendicular field components, and thus it could excite the dark ENZ mode of the ITO film even at normal incidence. Even with the coupling effect, the magnetic dipole resonance response of the SRR-ITO metasurface under $x$-polarized illumination is still persistent across both resonance branches (see Supporting Information Note 2.1). Strong surface currents are induced at both the ITO and SRR surfaces, especially on their contact area. Under the $y$-polarized illumination, the SRR metasurface exhibits no resonance within the wavelength range of interest, while the SRR-ITO metasurface has a weak electric-dipole-like resonance around 1560 nm wavelength (see Supporting Information Note 2.2). Unlike the magnetic dipole resonance, the electric-dipole-like resonance did not generate a detectable level of THz radiation in our experiments, which is attributed to the symmetry of the corresponding current distribution.[23,45]

**Enhanced Broadband THz Generation.** To characterize the performance of the hybrid nonlinear metasurface, we utilized a pump-wavelength-tunable THz time-domain spectroscopy (TDS) system to measure the generated THz waves with electro-optical sampling in a 1.0 mm-thick 110-cut ZnTe crystal (see Supporting Information Note 3.1). Figure 2d shows the measured normalized single-cycle THz pulses ($E_{THz}$, left) and the corresponding Fourier-transformed (frequency-domain) normalized intensity spectra (proportional to $|E_{THz}|^2$, right) generated from the SRR-ITO metasurface, the SRR


https://doi.org/10.1021/acs.nanolett.1c02372
Nano Lett. 2021, 21, 7699−7707

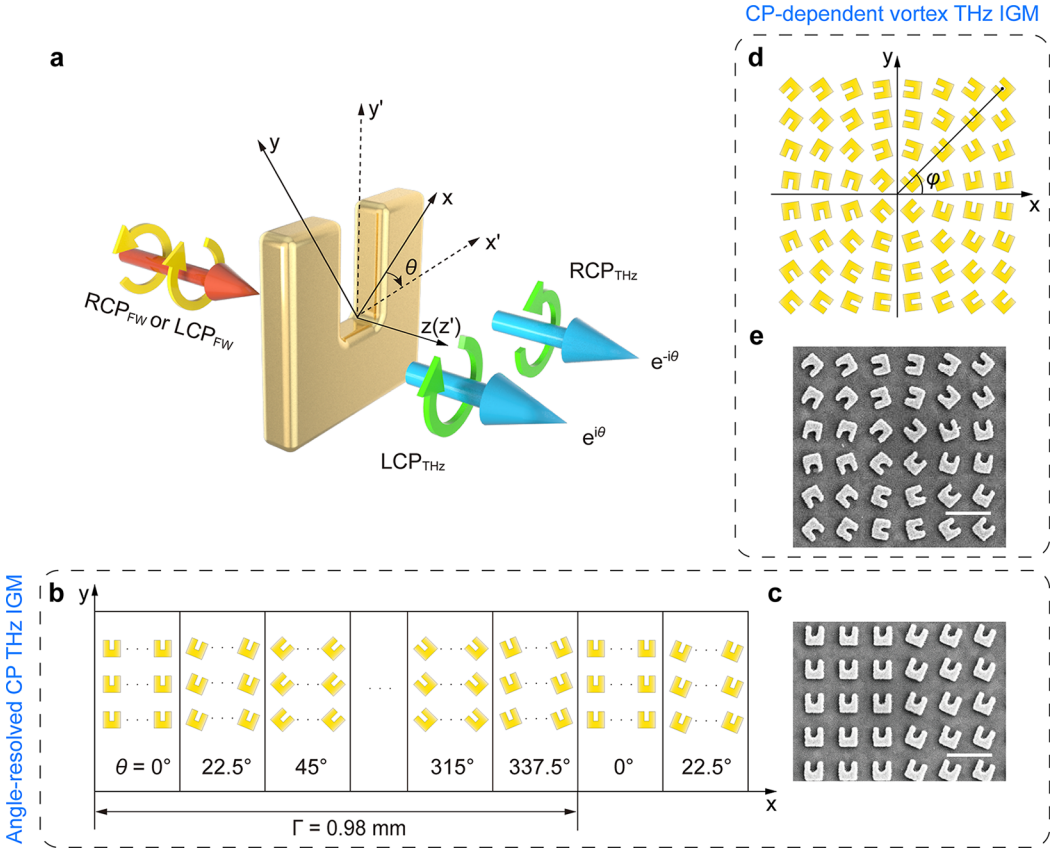


**Figure 3.** THz nonlinear Pancharatnam-Berry phase and design of the angle-resolved CP THz IGM and the CP-dependent vortex THz IGM. (a) Schematic of the nonlinear PB phases of the emitted CP THz waves under CP FW pumping. *x*-*y* and *x*′-*y*′ are the laboratory and local coordinates of the SRR, respectively. The two coordinate systems have a relative rotation angle of $\theta$. Here, the positive direction of $\theta$ is defined as the clockwise direction. Under CP FW pumping (regardless of the pump polarization's handedness), the emitted RCP THz wave acquires a $-\theta$ nonlinear PB phase, whereas the emitted LCP THz wave acquires a $+\theta$ nonlinear PB phase. (b) Design and (c) partial SEM image of the angle-resolved CP THz IGM (IGM1), where the SRR groups rotate linearly along the *x*-direction in 22.5° steps. (d) Design and (e) partial SEM image of the CP-dependent vortex THz IGM (IGM2), where the SRRs rotate linearly with their azimuthal position $\varphi$ according to $\theta = -\varphi$. Scale bars: 500 nm.

metasurface, and a bare identical ITO film, respectively. They are all excited from the substrate side by *x*-polarized normally incident pulses with 60 fs pulse width, 1.0 kHz repetition frequency, 1432 nm central wavelength, and 147.3 $\mu$J cm$^{-2}$ pump fluence. Clearly, the SRR-ITO metasurface generates the strongest THz signal, while the THz signal from the SRR metasurface is very weak but detectable. In both cases, the THz pulse duration is <2 ps, but the peak-to-peak amplitude ratio between them is about 100, indicating the critical role of the ITO film. For the bare ITO film, no THz signal is observed at normal incidence.[42] This clearly shows that the dominant contribution to the THz generation is from hybridization of the metasurface and the ITO film. To gain deeper understanding of the experimental results, nonlinear numerical simulations based on a Maxwell-hydrodynamic model are carried out (see Supporting Information Note 4.1).[46] The THz generation is observed to mainly occur in the vicinity of the SRR-ITO interface where the synthetic field enhancement by the plasmonic resonance and the ENZ mode is the strongest (see Supporting Information Note 4.2), and the coupling between the resonance of the SRR and the ENZ mode of the ITO film also plays an important role, where smaller coupling results in smaller THz amplitude (see Supporting Information Note 4.3, where a $SiO_2$ spacer is sandwiched between the SRR and the ITO film to tune the coupling). The measured THz bandwidth of the SRR-ITO metasurface above the high-frequency noise level is almost 4 THz. This is mainly restricted by the pulse duration of the excitation beam and the Reststrahlen-region absorption of the ZnTe crystal.[23] The spectral maximum of the THz radiation generated by the SRR-ITO metasurface (at 0.84 THz) is ~40 dB ($1 \times 10^4$ times) larger than that generated by the SRR metasurface (at 1.33 THz).

To explore the mechanism of the THz generation further, pump-wavelength-dependent measurements of the peak-to-peak amplitudes of the SRR-ITO metasurface and the SRR metasurface are performed in a pump wavelength range of 1200 to 2000 nm at a fixed pump fluence of 147.3 $\mu$J cm$^{-2}$, as shown in Figure 2e. Because of the magnetic resonance feature, THz generation is observed throughout the whole resonance range. The pump wavelength at which the THz amplitude reaches its maximum is not at the $\lambda_{ENZ}$ but close to one of the transmission dips of the linear spectrum. This can be attributed to the coupling-induced hybridized resonances of the SRR-ITO metasurface, where the plasmonic field enhancement is strong at frequencies both around the $\lambda_{ENZ}$ and around the resonance dips. As a result, the field enhancement and thus the THz amplitude is not the strongest at the $\lambda_{ENZ}$. This feature is also well reproduced by the nonlinear numerical simulations (see Supporting Information Note 4.4). Figure 2f shows the measured pump-fluence-dependence of the generated THz peak-to-peak amplitude for the SRR-ITO metasurface at 1360


https://doi.org/10.1021/acs.nanolett.1c02372
Nano Lett. 2021, 21, 7699−7707

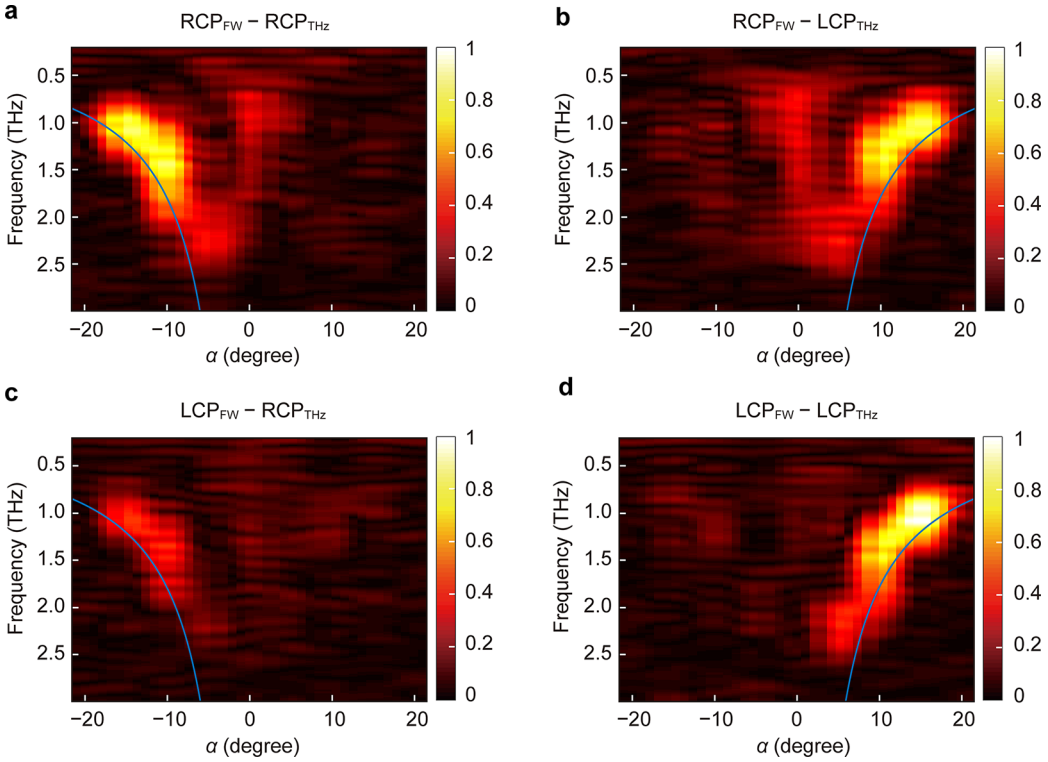


**Figure 4.** Measured THz generation by the angle-resolved CP THz IGM. Measured angle-resolved spectral dependence of the RCP and LCP THz emission amplitudes under (a, b) RCP and (c, d) LCP FW pumping, respectively. The pumps are normally incident at 1300 nm wavelength in all cases. All results are normalized to their common amplitude maximum. The blue lines are calculated from the generalized Snell's law. Regardless of RCP or LCP FW pumping, the IGM emits RCP THz waves toward negative angles, whereas LCP THz waves toward positive angles.

nm pump wavelength (where the generated THz peak-to-peak amplitude is the largest) and pump fluences ranging from 10.5 to 94.5 $\mu$J cm$^{-2}$. We observe a linear relation, revealing a second-order nonlinearity of the THz generation, $P_{THz} = \varepsilon_0\chi^{(2)}E_{FW,1}E^*_{FW,2} \propto \varepsilon_0\chi^{(2)}I_{FW}$.[47] Here, $P_{THz}$ is the THz polarization that is proportional to the generated THz electric field amplitude, $\varepsilon_0$ is the vacuum permittivity, $\chi^{(2)}$ is the effective second-order nonlinear susceptibility, $E_{FW,1}$ and $E_{FW,2}$ represent the electric fields with two arbitrary frequency components of $\omega_{FW,1}$ and $\omega_{FW,2}$ in the FW spectrum whose frequency difference equals the generated THz frequency with $\omega_{THz} = \omega_{FW,1} - \omega_{FW,2}$, and $I_{FW}$ is the pump fluence. It should be noted that the fitting line does not go through the origin, possibly due to the measuring threshold of our TDS system. To benchmark the hybrid nonlinear metasurface as a practical THz generator, the pump-fluence-dependent THz peak-to-peak amplitude from a ZnTe crystal with thickness matching the coherence length (0.2 mm) in the NIR regime was also measured under the same pump condition, as well as that from a conventional 1.0 mm thick ZnTe crystal at 800 nm pump wavelength, as shown in Figure 2f. Despite being more than 3000 (15000) times thinner, the conversion efficiency of the ∼66 nm thick SRR-ITO metasurface approaches 84% (50%) of that of the 0.2 (1.0) mm thick ZnTe crystal.

In addition, polarization-resolved measurements (see Supporting Information Note 3.2) show that the THz waves generated by the metasurfaces have linear *y*-polarization (along the SRR gap) under *x*-polarized pumping (perpendicular to the SRR gap), which is consistent with previous reports.[23] Therefore, the measured THz signals in Figure 2d−f are all *y*-polarized.

**Nonlinear Pancharatnam-Berry Phase of the Meta-Atom.** PB phase is a robust phase control method for CP light, which is dependent on the rotation angle of the meta-atom $\theta$ and is intrinsically broadband.[48] In the linear regime, the PB phase between incident and transmitted CP waves of opposite handedness is $2\theta$ for right-handed CP (RCP) and $-2\theta$ for left-handed CP (LCP) incident waves. The concept of PB phase has recently been extended into the nonlinear optical regime for harmonic generation,[49,50] wave mixing,[51] and difference frequency generation,[52] and the corresponding nonlinear PB phase is modified depending on the order of the nonlinear process. For an SRR with an orientation angle $\theta$ pumped by a normally incident FW (Figure 3a), the emitted THz wave can always be decomposed into an RCP THz component (RCP$_{THz}$) and an LCP THz component (LCP$_{THz}$). Regardless of the handedness of the CP pump beam, the generated RCP and LCP THz components acquire a $\phi^{RCP}_{THz} = -\theta$ and a $\phi^{LCP}_{THz} = +\theta$ nonlinear PB phases, respectively. This is true for every difference frequency generation process among the pump spectrum, so the nonlinear PB phases here are naturally broadband for the emitted THz wave. A detailed derivation can be found in Supporting Information Note 5. This means that the nonlinear PB phase of the emitted CP THz wave is controlled merely by the rotation angle $\theta$, in sharp contrast to the FW-handedness-dependent nonlinear PB phase in harmonic generation processes.[49,50] Under CP pumping, the amplitudes of the emitted CP THz waves are uniform with respect to $\theta$.

**Angle-Resolved CP THz IGM.** The nonlinear PB phase of the nonlinear metasurface is engineered to realize an angle-resolved CP THz IGM (IGM1, see Figure 1c). By gradually changing the orientations of the meta-atoms linearly along a


https://doi.org/10.1021/acs.nanolett.1c02372
Nano Lett. 2021, 21, 7699−7707

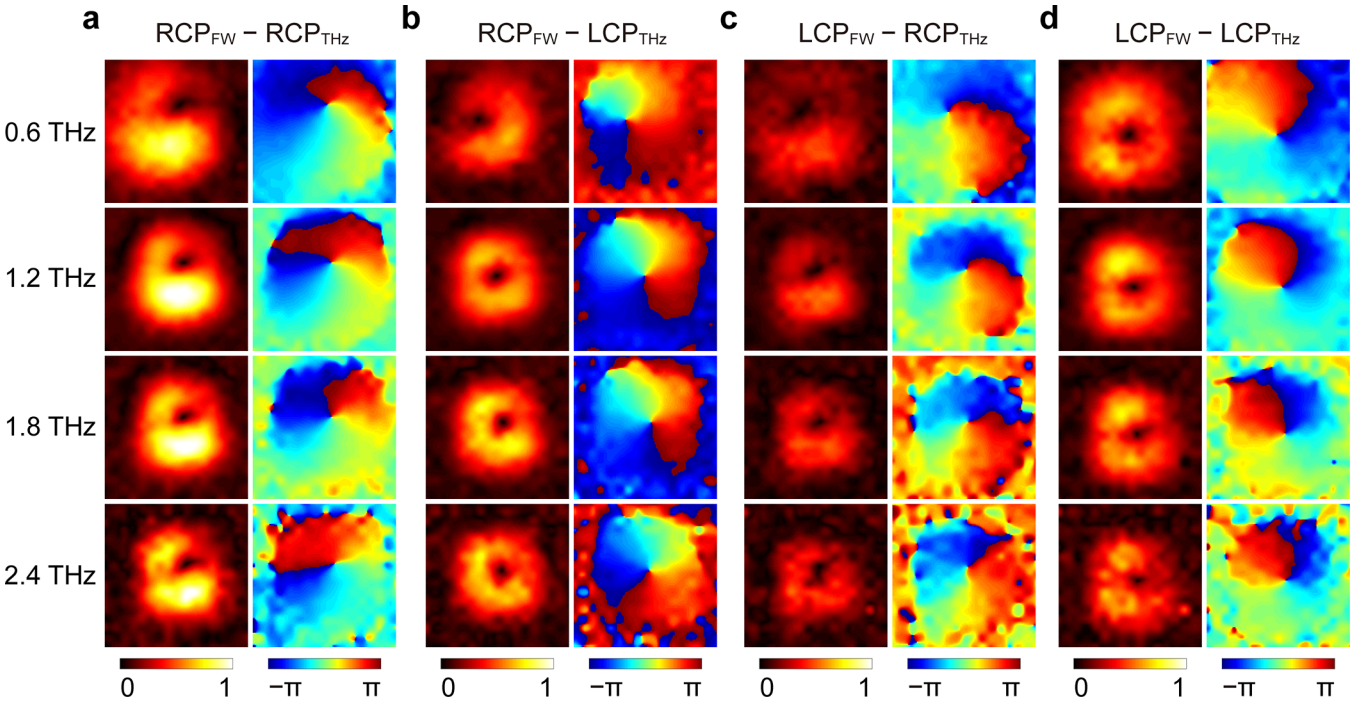


**Figure 5.** Measured THz beam profiles for the CP-dependent vortex THz IGM. Measured RCP and LCP THz beam amplitude (left) and phase (right) profiles at 0.6, 1.2, 1.8, and 2.4 THz under (a, b) RCP and (c, d) LCP FW pumping, respectively. The pump is normally incident with 1300 nm wavelength in all cases. All the amplitude profiles at the same frequency are normalized to their common amplitude maximum. Irrespective of RCP or LCP FW pumping, the IGM emits RCP THz beams carrying orbital angular momentum of $l$ = +1 and LCP THz beams carrying orbital angular momentum of $l$ = −1.

certain direction, the metasurface can be designed to provide opposite linear phase gradients for the emitted broadband RCP$_{THz}$ and LCP$_{THz}$. As schematically illustrated in Figure 3b, the supercell of IGM1 is composed of 16 groups of meta-atoms. The rotation angle of the meta-atoms increases from group to group along the $x$-direction in 22.5° steps. Such a design creates a constant phase gradient $\frac{d\phi_{THz}^{RCP}}{dx} = -\frac{2\pi}{\Gamma}$ for the emitted RCP$_{THz}$, while $\frac{d\phi_{THz}^{LCP}}{dx} = \frac{2\pi}{\Gamma}$ for the emitted LCP$_{THz}$. According to the generalized Snell's law,[16] under pumping at normal incidence, the CP THz wave is emitted at an angle of $\alpha = \sin^{-1}\left(\frac{c}{2\pi f_{THz}}\frac{d\phi_{THz}^{RCP/LCP}}{dx}\right)$, located at negative and positive angles for RCP$_{THz}$ and LCP$_{THz}$, respectively.

To demonstrate IGM1, we fabricate a 3.9 mm × 1.0 mm sample (see Methods) and measure its angle-resolved CP THz generation under normally incident RCP$_{FW}$ and LCP$_{FW}$ pumping (see Supporting Information Note 3.3). Figure 3c shows a partial scanning electron microscope image of the fabricated IGM1. The super period is Γ = 0.98 mm. Here, the larger sample dimension along the direction of the phase gradient increases the angle resolution of the emitted CP THz waves according to Fourier optics. The frequency-domain CP THz amplitudes as a function of the emission angle are measured under laser pumping with 1300 nm wavelength and 111.8 $\mu$J cm$^{-2}$ fluence. As shown by Figure 4, both RCP$_{THz}$ (Figure 4a, c) and LCP$_{THz}$ (Figure 4b, d) are emitted simultaneously with opposite emission angles that do not depend on the handedness of the CP pump beam (Figure 4a, b for RCP$_{FW}$ and Figure 4c, d for LCP$_{FW}$). RCP$_{THz}$ and LCP$_{THz}$ both span a frequency range of more than 2.0 THz. The THz emission angles are in good agreement with the generalized Snell's law (blue lines). THz frequencies below 0.6 THz could not be detected due to the limited numerical aperture of the collection component in our measuring system, while those above 2.6 THz were not detected because of the reduced THz amplitude caused by a 5.0 mm slit employed for angle-resolved detection. The results confirm that the introduced nonlinear PB phase controlled by meta-atom orientations can functionally tailor the overall wavefront of the THz beam and thus give rise to predesigned THz emission.

**CP-Dependent Vortex THz IGM.** THz vortex beams carrying spin angular momentum $s$ and orbital angular momentums $l$ can be applied to ultrafast multichannel wireless communication. Broadband vortex-based THz spectroscopy is promising to reveal unique material information, such as the spin and orbital contributions to magnetism.[53,54] Spins $s$ = −1 and +1 correspond to RCP and LCP, whereas $l$ is the topological charge of the vortex beam. Here we design a CP-dependent vortex THz IGM (IGM2), allowing simultaneous emission of broadband vortex THz beams carrying spin angular momentum and orbital angular momentum of ($s$, $l$) = (−1, +1) and (+1, −1) as shown in Figure 1d. As schematically illustrated in Figure 3d, IGM2 is composed of meta-atoms with different rotation angles $\theta$ for different azimuthal positions $\varphi$ on the metasurface, where $\theta = -\varphi$. This creates a positive azimuthal phase gradient (counterclockwise) for the RCP$_{THz}$ with $l = \frac{d\phi_{THz}^{RCP}}{d\varphi} = 1$ and a negative azimuthal phase gradient (clockwise) for the LCP$_{THz}$ with $l = \frac{d\phi_{THz}^{LCP}}{d\varphi} = -1$. Such a phase distribution for vortex beam generation is similar to that using linear metasurfaces.[16,17] Figure 3e shows a partial scanning electron microscope image of the central area of IGM2. The whole sample area is 0.6 mm × 0.6 mm.



https://doi.org/10.1021/acs.nanolett.1c02372
Nano Lett. 2021, 21, 7699−7707

To characterize the performance of IGM2, we measure the spatial amplitude and phase distributions of the emitted THz beam by scanning IGM2 using the TDS system with 1300 nm CP laser pumping (see Supporting Information Note 3.4). Figure 5 shows the measurement results at four exemplary frequencies (0.6, 1.2, 1.8, and 2.4 THz from top to bottom) illustrating the broadband operation. All amplitude distributions show donut-shaped beam profiles, while all phase distributions show a $|l| = 1$ vortex as indicated by the phase singularities surrounded by ±360° helical phase loops. Regardless of the handedness of the CP pump beam, an $RCP_{THz}$ vortex beam with $l = +1$ (Figure 5a, c) and an $LCP_{THz}$ vortex beam with $l = -1$ (Figure 5b,d) are generated. The size of the vortex beam decreases gradually from 0.6 to 2.4 THz because of a smaller divergence angle for shorter wavelengths. As the $RCP_{THz}$ and $LCP_{THz}$ vortex beams fully overlap with each other, they combine to form a vector beam. On the other hand, one may choose to spatially separate the two CP components by combining the two phase profiles, one for generating the vortex beams and the other for beam deflection.

## CONCLUSION

In summary, we have successfully demonstrated a hybrid nonlinear metasurface composed of plasmonic SRR meta-atoms and ITO film, which seamlessly combines the functionalities of efficient THz generation and THz manipulation. This allows simultaneous tailoring of the polarization and wavefront of the emitted THz beams over a broadband frequency range. Our proposed nonlinear THz IGMs open a gateway toward developing next-generation, low-working-power, efficient, compact, and ultrafast THz photonic devices.

## METHODS

**Nonlinear Metasurface Fabrication.** The SRR-ITO and SRR metasurfaces were fabricated using electron beam lithography (EBL) and electron beam evaporation. First, the substrates were cleaned using acetone in an ultrasonic cleaner. Second, an ∼300 nm thick ZEP-520 electron resist layer was spin-coated onto the substrates and subsequently baked at a temperature of 160 °C for 5 min. Then, a conductive polymer layer was spin-coated onto the substrates followed by baking at a temperature of 90 °C for 1 min to avoid structure distortion from charge accumulation. Next, the metasurface patterns were written onto the resist layer using EBL (JEOL 6300FS) and ZEP-N50 development. Next, films of 3 nm Ti and 40 nm Au were successively deposited by e-beam evaporation. Finally, the metasurfaces were obtained after lift-off and cleaning processes.

**Transmission Measurements of the Metasurfaces.** The polarization-dependent transmission spectra of the SRR-ITO metasurface and the SRR metasurface were measured using a custom-built spectroscopy system. NIR light emitted from a stabilized tungsten IR light source (Thorlabs, SLS202L/M) was first focused onto the metasurface by an objective lens (×40, 0.65 NA). Then, the transmitted light was collected and collimated into a spectrometer (Princeton Instruments, Acton SpectraPro SP-2300) for spectral measurements. The polarization of incident light was controlled by a broadband NIR polarizer. The polarization-dependent transmission spectra were obtained by normalizing the measured spectrum of each metasurface to that of an unpatterned reference area on the same substrate.

## ASSOCIATED CONTENT

### Supporting Information

The Supporting Information is available free of charge at https://pubs.acs.org/doi/10.1021/acs.nanolett.1c02372.

(1) Theoretical fitting of the transmission spectra; (2) resonance features of the SRR-ITO metasurface; (3) experimental measurements; (4) simulations of the enhanced THz generation; (5) derivation of the nonlinear PB phase for the THz emission (PDF)

## AUTHOR INFORMATION


### Corresponding Authors

**Xueqian Zhang** − *Center for Terahertz Waves and College of Precision Instrument and Optoelectronics Engineering, Tianjin University and the Key Laboratory of Optoelectronics Information and Technology (Ministry of Education), Tianjin 300072, China;* orcid.org/0000-0001-7712-3365; Email: alearn1988@tju.edu.cn

**Ming Fang** − *Key Laboratory of Intelligent Computing and Signal Processing, Ministry of Education, Anhui University, Hefei 230039, China*; Email: mingfang@ahu.edu.cn

**Shuang Zhang** − *Department of Physics, Faculty of Science, University of Hong Kong, Hong Kong 999077, China;* orcid.org/0000-0003-4556-2333; Email: shuzhang@hku.hk

**Jiaguang Han** − *Center for Terahertz Waves and College of Precision Instrument and Optoelectronics Engineering, Tianjin University and the Key Laboratory of Optoelectronics Information and Technology (Ministry of Education), Tianjin 300072, China*; Email: jiaghan@tju.edu.cn

### Authors

**Yongchang Lu** − *Center for Terahertz Waves and College of Precision Instrument and Optoelectronics Engineering, Tianjin University and the Key Laboratory of Optoelectronics Information and Technology (Ministry of Education), Tianjin 300072, China; Physical Science and Engineering Division, King Abdullah University of Science and Technology (KAUST), Thuwal 23955-6900, Saudi Arabia*

**Xi Feng** − *Center for Terahertz Waves and College of Precision Instrument and Optoelectronics Engineering, Tianjin University and the Key Laboratory of Optoelectronics Information and Technology (Ministry of Education), Tianjin 300072, China; Physical Science and Engineering Division, King Abdullah University of Science and Technology (KAUST), Thuwal 23955-6900, Saudi Arabia*

**Qingwei Wang** − *Center for Terahertz Waves and College of Precision Instrument and Optoelectronics Engineering, Tianjin University and the Key Laboratory of Optoelectronics Information and Technology (Ministry of Education), Tianjin 300072, China; Physical Science and Engineering Division, King Abdullah University of Science and Technology (KAUST), Thuwal 23955-6900, Saudi Arabia*

**Wei E.I. Sha** − *Key Laboratory of Micro-nano Electronic Devices and Smart Systems of Zhejiang Province, College of Information Science & Electronic Engineering, Zhejiang University, Hangzhou 310027, China;* orcid.org/0000-0002-7431-8121

**Zhixiang Huang** − *Key Laboratory of Intelligent Computing and Signal Processing, Ministry of Education, Anhui University, Hefei 230039, China*




https://doi.org/10.1021/acs.nanolett.1c02372
Nano Lett. 2021, 21, 7699−7707

**Quan Xu** − *Center for Terahertz Waves and College of Precision Instrument and Optoelectronics Engineering, Tianjin University and the Key Laboratory of Optoelectronics Information and Technology (Ministry of Education), Tianjin 300072, China;* orcid.org/0000-0001-9246-3253

**Li Niu** − *Center for Terahertz Waves and College of Precision Instrument and Optoelectronics Engineering, Tianjin University and the Key Laboratory of Optoelectronics Information and Technology (Ministry of Education), Tianjin 300072, China*

**Xieyu Chen** − *Center for Terahertz Waves and College of Precision Instrument and Optoelectronics Engineering, Tianjin University and the Key Laboratory of Optoelectronics Information and Technology (Ministry of Education), Tianjin 300072, China*

**Chunmei Ouyang** − *Center for Terahertz Waves and College of Precision Instrument and Optoelectronics Engineering, Tianjin University and the Key Laboratory of Optoelectronics Information and Technology (Ministry of Education), Tianjin 300072, China;* orcid.org/0000-0002-9413-9630

**Yuanmu Yang** − *State Key Laboratory of Precision Measurement Technology and Instruments, Department of Precision Instrument, Tsinghua University, Beijing 100084, China;* orcid.org/0000-0002-5264-0822

**Xixiang Zhang** − *Physical Science and Engineering Division, King Abdullah University of Science and Technology (KAUST), Thuwal 23955-6900, Saudi Arabia;* orcid.org/0000-0002-3478-6414

**Eric Plum** − *Optoelectronics Research Centre and Centre for Photonic Metamaterials, University of Southampton, Highfield, Southampton SO17 1BJ, United Kingdom;* orcid.org/0000-0002-1552-1840

**Weili Zhang** − *School of Electrical and Computer Engineering, Oklahoma State University, Stillwater, Oklahoma 74078, United States*

Complete contact information is available at: https://pubs.acs.org/10.1021/acs.nanolett.1c02372

### Author Contributions

†Y.L., X.F., and Q.W. contributed equally to this work. XQ.Z. and J.H. conceived the idea; Y.L., X.F., Q.W., and XX.Z fabricated the samples; Y.L., X.F., and Q.W. performed the measurements; M.F. carried out the numerical simulations; Y.L., X.F., Q.W., XQ.Z., M.F., Q.X., L.N., X.C. Y.Y., E.P., and J.H. analyzed the data; W.S. and Z.H. suggested on the theory; XQ.Z., S.Z., J.H., and W.Z. supervised the project; all the authors discussed the results and prepared the manuscript.

### Notes

The authors declare no competing financial interest.

## ■ ACKNOWLEDGMENTS

This work is supported by the National Key Research and Development Program of China (Grant 2017YFA0701004); the National Natural Science Foundation of China (Grants 61735012, 62025504, 62075158, 11974259, 61875150, 61935015, 62005193, 61901001, U20A20164, 61971001, 61975177, and 62135008); the Tianjin Municipal Fund for Distinguished Young Scholars (18JCJQJC45600); the UK's Engineering and Physical Sciences Research Council (Grants EP/M009122/1 and EP/T02643X/1); the Research Grants Council of Hong Kong (AoE/P-701/20). The authors acknowledge the High-performance Computing Platform of Anhui University for providing computing resources. Following a period of embargo, the data from this paper will be available from the University of Southampton ePrints research repository: https://doi.org/10.5258/SOTON/D1948.

## ■ REFERENCES

(1) Tonouchi, M. Cutting-edge terahertz technology. *Nat. Photonics* **2007**, *1*, 97−105.

(2) Kim, P.-J.; Jeong, J.-H.; Jazbinsek, M.; Choi, S.-B.; Baek, I.-H.; Kim, J.-T.; Rotermund, F.; Yun, H.; Lee, Y. S.; Günter, P.; Kwon, O.-P. Highly Efficient Organic THz Generator Pumped at Near-Infrared: Quinolinium Single Crystals. *Adv. Funct. Mater.* **2012**, *22*, 200−209.

(3) Vicario, C.; Monoszlai, B.; Hauri, C. P. GV/m Single-Cycle Terahertz Fields from a Laser-Driven Large-Size Partitioned Organic Crystal. *Phys. Rev. Lett.* **2014**, *112*, 213901.

(4) Seifert, T.; Jaiswal, S.; Martens, U.; Hannegan, J.; Braun, L.; Maldonado, P.; Freimuth, F.; Kronenberg, A.; Henrizi, J.; Radu, I.; Beaurepaire, E.; Mokrousov, Y.; Oppeneer, P. M.; Jourdan, M.; Jakob, G.; Turchinovich, D.; Hayden, L. M.; Wolf, M.; Munzenberg, M.; Klaui, M.; Kampfrath, T. Efficient metallic spintronic emitters of ultrabroadband terahertz radiation. *Nat. Photonics* **2016**, *10*, 483−488.

(5) Qiu, H. S.; Zhou, L. F.; Zhang, C. H.; Wu, J. B.; Tian, Y. Z.; Cheng, S. D.; Mi, S. B.; Zhao, H. B.; Zhang, Q.; Wu, D.; Jin, B. B.; Chen, J.; Wu, P. H. Ultrafast spin current generated from an antiferromagnet. *Nat. Phys.* **2021**, *17*, 388−394.

(6) Yao, X. H.; Tokman, M.; Belyanin, A. Efficient Nonlinear Generation of THz Plasmons in Graphene and Topological Insulators. *Phys. Rev. Lett.* **2014**, *112*, 055501.

(7) Gao, Y.; Kaushik, S.; Philip, E. J.; Li, Z.; Qin, Y.; Liu, Y. P.; Zhang, W. L.; Su, Y. L.; Chen, X.; Weng, H.; et al. Chiral terahertz wave emission from the Weyl semimetal TaAs. *Nat. Commun.* **2020**, *11*, 720.

(8) Berry, C. W.; Wang, N.; Hashemi, M. R.; Unlu, M.; Jarrahi, M. Significant performance enhancement in photoconductive terahertz optoelectronics by incorporating plasmonic contact electrodes. *Nat. Commun.* **2013**, *4*, 1622.

(9) Wang, Q.; Plum, E.; Yang, Q.; Zhang, X.; Xu, Q.; Xu, Y.; Han, J.; Zhang, W. Reflective chiral meta-holography: multiplexing holograms for circularly polarized waves. *Light: Sci. Appl.* **2018**, *7*, 25.

(10) Xu, Y. H.; Li, Q.; Zhang, X. Q.; Wei, M. G.; Xu, Q.; Wang, Q.; Zhang, H. F.; Zhang, W. T.; Hu, C.; Zhang, Z. W.; Zhang, C. L.; Zhang, X. X.; Han, J. G.; Zhang, W. L. Spin-Decoupled Multifunctional Metasurface for Asymmetric Polarization Generation. *ACS Photonics* **2019**, *6*, 2933−2941.

(11) Tian, H. W.; Shen, H. Y.; Zhang, X. G.; Li, X.; Jiang, W. X.; Cui, T. J. Terahertz Metasurfaces: Toward Multifunctional and Programmable Wave Manipulation. *Front. Phys.* **2020**, *8*, 584077.

(12) Cong, L. Q.; Cao, W.; Zhang, X. Q.; Tian, Z.; Gu, J. Q.; Singh, R.; Han, J. G.; Zhang, W. L. A perfect metamaterial polarization rotator. *Appl. Phys. Lett.* **2013**, *103*, 171107.

(13) Zhang, X. Q.; Tian, Z.; Yue, W. S.; Gu, J. Q.; Zhang, S.; Han, J. G.; Zhang, W. L. Broadband Terahertz Wave Deflection Based on C-shape Complex Metamaterials with Phase Discontinuities. *Adv. Mater.* **2013**, *25*, 4567−4572.

(14) Cong, L.; Xu, N.; Han, J.; Zhang, W.; Singh, R. A Tunable Dispersion-Free Terahertz Metadevice with Pancharatnam−Berry-Phase-Enabled Modulation and Polarization Control. *Adv. Mater.* **2015**, *27*, 6630−6636.

(15) Cong, L.; Pitchappa, P.; Wang, N.; Singh, R. Electrically Programmable Terahertz Diatomic Metamolecules for Chiral Optical Control. *Research* **2019**, *2019*, 7084251.

(16) Yu, N. F.; Genevet, P.; Kats, M. A.; Aieta, F.; Tetienne, J. P.; Capasso, F.; Gaburro, Z. Light Propagation with Phase Discontinuities: Generalized Laws of Reflection and Refraction. *Science* **2011**, *334*, 333−337.

(17) Sun, S.; He, Q.; Hao, J.; Xiao, S.; Zhou, L. Electromagnetic metasurfaces: physics and applications. *Adv. Opt. Photonics* **2019**, *11*, 380−479.
(18) Li, G.; Zhang, S.; Zentgraf, T. Nonlinear photonic metasurfaces. *Nat. Rev. Mater.* **2017**, *2*, 17010.
(19) Sain, B.; Meier, C.; Zentgraf, T. Nonlinear optics in all-dielectric nanoantennas and metasurfaces: a review. *Adv. Photonics* **2019**, *1*, 024002.
(20) Klein, M. W.; Enkrich, C.; Wegener, M.; Linden, S. Second-harmonic generation from magnetic metamaterials. *Science* **2006**, *313*, 502−504.
(21) Yang, Y. M.; Wang, W. Y.; Boulesbaa, A.; Kravchenko, I. I.; Briggs, D. P.; Puretzky, A.; Geohegan, D.; Valentine, J. Nonlinear Fano-Resonant Dielectric Metasurfaces. *Nano Lett.* **2015**, *15*, 7388−7393.
(22) Koshelev, K.; Kruk, S.; Melik-Gaykazyan, E.; Choi, J. H.; Bogdanov, A.; Park, H. G.; Kivshar, Y. Subwavelength dielectric resonators for nonlinear nanophotonics. *Science* **2020**, *367*, 288−292.
(23) Luo, L.; Chatzakis, I.; Wang, J.; Niesler, F. B.; Wegener, M.; Koschny, T.; Soukoulis, C. M. Broadband terahertz generation from metamaterials. *Nat. Commun.* **2014**, *5*, 3055.
(24) Keren-Zur, S.; Tal, M.; Fleischer, S.; Mittleman, D. M.; Ellenbogen, T. Generation of spatiotemporally tailored terahertz wavepackets by nonlinear metasurfaces. *Nat. Commun.* **2019**, *10*, 1778.
(25) Minerbi, E.; Keren-Zur, S.; Ellenbogen, T. Nonlinear Metasurface Fresnel Zone Plates for Terahertz Generation and Manipulation. *Nano Lett.* **2019**, *19*, 6072−6077.
(26) Lee, J.; Tymchenko, M.; Argyropoulos, C.; Chen, P. Y.; Lu, F.; Demmerle, F.; Boehm, G.; Amann, M. C.; Alu, A.; Belkin, M. A. Giant nonlinear response from plasmonic metasurfaces coupled to intersubband transitions. *Nature* **2014**, *511*, 65−69.
(27) Fedotova, A.; Younesi, M.; Sautter, J.; Vaskin, A.; Lochner, F. J. F.; Steinert, M.; Geiss, R.; Pertsch, T.; Staude, I.; Setzpfandt, F. Second-Harmonic Generation in Resonant Nonlinear Metasurfaces Based on Lithium Niobate. *Nano Lett.* **2020**, *20*, 8608−8614.
(28) Zhang, S.; Li, G. C.; Chen, Y. Q.; Zhu, X. P.; Liu, S. D.; Lei, D. Y.; Duan, H. G. Pronounced Fano Resonance in Single Gold Split Nanodisks with 15 nm Split Gaps for Intensive Second Harmonic Generation. *ACS Nano* **2016**, *10*, 11105−11114.
(29) Koshelev, K.; Tang, Y.; Li, K.; Choi, D.-Y.; Li, G.; Kivshar, Y. Nonlinear Metasurfaces Governed by Bound States in the Continuum. *ACS Photonics* **2019**, *6*, 1639−1644.
(30) Kravets, V. G.; Kabashin, A. V.; Barnes, W. L.; Grigorenko, A. N. Plasmonic Surface Lattice Resonances: A Review of Properties and Applications. *Chem. Rev.* **2018**, *118*, 5912−5951.
(31) Chen, S. M.; Reineke, B.; Li, G. X.; Zentgraf, T.; Zhang, S. Strong Nonlinear Optical Activity Induced by Lattice Surface Modes on Plasmonic Metasurface. *Nano Lett.* **2019**, *19*, 6278−6283.
(32) Reshef, O.; De Leon, I.; Alam, M. Z.; Boyd, R. W. Nonlinear optical effects in epsilon-near-zero media. *Nat. Rev. Mater.* **2019**, *4*, 535−551.
(33) Kinsey, N.; DeVault, C.; Boltasseva, A.; Shalaev, V. M. Near-zero-index materials for photonics. *Nat. Rev. Mater.* **2019**, *4*, 742−760.
(34) Alam, M. Z.; De Leon, I.; Boyd, R. W. Large optical nonlinearity of indium tin oxide in its epsilon-near-zero region. *Science* **2016**, *352*, 795−797.
(35) Capretti, A.; Wang, Y.; Engheta, N.; Dal Negro, L. Comparative Study of Second-Harmonic Generation from Epsilon-Near-Zero Indium Tin Oxide and Titanium Nitride Nanolayers Excited in the Near-Infrared Spectral Range. *ACS Photonics* **2015**, *2*, 1584−1591.
(36) Caspani, L.; Kaipurath, R. P.; Clerici, M.; Ferrera, M.; Roger, T.; Kim, J.; Kinsey, N.; Pietrzyk, M.; Di Falco, A.; Shalaev, V. M.; Boltasseva, A.; Faccio, D. Enhanced Nonlinear Refractive Index in epsilon-Near-Zero Materials. *Phys. Rev. Lett.* **2016**, *116*, 233901.
(37) Khurgin, J. B.; Clerici, M.; Bruno, V.; Caspani, L.; DeVault, C.; Kim, J.; Shaltout, A.; Boltasseva, A.; Shalaev, V. M.; Ferrera, M.; Faccio, D.; Kinsey, N. Adiabatic frequency shifting in epsilon-near-zero materials: the role of group velocity. *Optica* **2020**, *7*, 226−231.
(38) Yang, Y. M.; Lu, J.; Manjavacas, A.; Luk, T. S.; Liu, H. Z.; Kelley, K.; Maria, J. P.; Runnerstrom, E. L.; Sinclair, M. B.; Ghimire, S.; Brener, I. High-harmonic generation from an epsilon-near-zero material. *Nat. Phys.* **2019**, *15*, 1022−1026.
(39) Alam, M. Z.; Schulz, S. A.; Upham, J.; De Leon, I.; Boyd, R. W. Large optical nonlinearity of nanoantennas coupled to an epsilon-near-zero material. *Nat. Photonics* **2018**, *12*, 79−83.
(40) Deng, J. H.; Tang, Y. T.; Chen, S. M.; Li, K. F.; Zayats, A. V.; Li, G. X. Giant Enhancement of Second-Order Nonlinearity of Epsilon-near-Zero Medium by a Plasmonic Metasurface. *Nano Lett.* **2020**, *20*, 5421−5427.
(41) Niu, X. X.; Hu, X. Y.; Sun, Q.; Lu, C. C.; Yang, Y. M.; Yang, H.; Gong, Q. H. Polarization-selected nonlinearity transition in gold dolmens coupled to an epsilon-near-zero material. *Nanophotonics* **2020**, *9*, 4839−4851.
(42) Jia, W.; Liu, M.; Lu, Y.; Feng, X.; Wang, Q.; Zhang, X.; Ni, Y.; Hu, F.; Gong, M.; Xu, X.; et al. Broadband terahertz wave generation from an epsilon-near-zero material. *Light: Sci. Appl.* **2021**, *10*, 11.
(43) Vassant, S.; Hugonin, J. P.; Marquier, F.; Greffet, J. J. Berreman mode and epsilon near zero mode. *Opt. Express* **2012**, *20*, 23971−23977.
(44) Campione, S.; Brener, I.; Marquier, F. Theory of epsilon-near-zero modes in ultrathin films. *Phys. Rev. B: Condens. Matter Mater. Phys.* **2015**, *91*, 121408.
(45) Fang, M.; Niu, K.; Huang, Z.; Sha, W. E. I.; Wu, X.; Koschny, T.; Soukoulis, C. M. Investigation of broadband terahertz generation from metasurface. *Opt. Express* **2018**, *26*, 14241−14250.
(46) Fang, M.; Huang, Z.; Sha, W. E. I.; Xiong, X. Y. Z.; Wu, X. Full hydrodynamic model of nonlinear electromagnetic response in metallic metamaterials. *Prog. Electromagn. Res.* **2016**, *157*, 63−78.
(47) Boyd, R. W. *Nonlinear Optics*, 3rd ed.; Academic Press: Cambridge, MA, 2008; pp 6−10.
(48) Huang, L. L.; Chen, X. Z.; Muhlenbernd, H.; Li, G. X.; Bai, B. F.; Tan, Q. F.; Jin, G. F.; Zentgraf, T.; Zhang, S. Dispersionless Phase Discontinuities for Controlling Light Propagation. *Nano Lett.* **2012**, *12*, 5750−5755.
(49) Li, G. X.; Chen, S. M.; Pholchai, N.; Reineke, B.; Wong, P. W. H.; Pun, E. Y. B.; Cheah, K. W.; Zentgraf, T.; Zhang, S. Continuous control of the nonlinearity phase for harmonic generations. *Nat. Mater.* **2015**, *14*, 607−612.
(50) Ye, W. M.; Zeuner, F.; Li, X.; Reineke, B.; He, S.; Qiu, C. W.; Liu, J.; Wang, Y. T.; Zhang, S.; Zentgraf, T. Spin and wavelength multiplexed nonlinear metasurface holography. *Nat. Commun.* **2016**, *7*, 11930.
(51) Li, G. X.; Sartorello, G.; Chen, S. M.; Nicholls, L. H.; Li, K. F.; Zentgraf, T.; Zhang, S.; Zayats, A. V. Spin and Geometric Phase Control Four-Wave Mixing from Metasurfaces. *Laser Photonics Rev.* **2018**, *12*, 1800034.
(52) McDonnell, C.; Deng, J.; Sideris, S.; Ellenbogen, T.; Li, G. Functional THz emitters based on Pancharatnam-Berry phase nonlinear metasurfaces. *Nat. Commun.* **2021**, *12*, 30.
(53) Sirenko, A. A.; Marsik, P.; Bernhard, C.; Stanislavchuk, T. N.; Kiryukhin, V.; Cheong, S. W. Terahertz Vortex Beam as a Spectroscopic Probe of Magnetic Excitations. *Phys. Rev. Lett.* **2019**, *122*, 237401.
(54) Sirenko, A. A.; Marsik, P.; Bugnon, L.; Soulier, M.; Bernhard, C.; Stanislavchuk, T. N.; Xu, X.; Cheong, S. W. Total angular momentum dichroism of the terahertz vortex beams at the antiferromagnetic resonances. *Phys. Rev. Lett.* **2021**, *126*, 157401.


https://doi.org/10.1021/acs.nanolett.1c02372
*Nano Lett.* 2021, 21, 7699−7707